Cooperative Optimization of Pre-swirl Nozzles and Receiver Holes in a Radial Pre-swirl System Using an ANN-PSO Approach

D. Wang[1], C. Song[2], C. Qiu[1], Y. Xu[3], W. Wang[3] and P. I. Mihailovich[1†]

[1] *Faculty of Aircraft, Rocket Engines and Power Plants, Moscow Aviation Institute, Moscow 125080, Russia*
[2] *Faculty of Aerospace, Moscow Aviation Institute, Moscow 125080, Russia*
[3] *Faculty of Aircraft Engineering, Moscow Aviation Institute, Moscow 125080, Russia*

†*Corresponding Author Email: platonov@mai.ru*

ABSTRACT

Radial pre-swirl systems are widely applied in the aviation industry to supply cooling air to high-pressure turbine blades in aircraft engines. The efficiency of the film cooling can significantly decline when the air pressure is insufficient. This study explored the synergistic optimization of pre-swirl nozzles and receiver holes to improve the pressure ratio of a radial pre-swirl system. To attain this objective, we established a surrogate model using an artificial neural network and adopted the particle swarm optimization algorithm to pinpoint the optimized geometric parameters within the defined design scope. The results revealed that the optimal performance was achieved when the pre-swirl-nozzle tangential angle reached 40.4368°, the receiver-hole axial angle reached 2.0286°, and the tangential angle reached 30°. Additionally, multiple computational simulations were performed under diverse operational conditions to validate the efficacy of this optimization. The results revealed a significant enhancement in the pressure-boosting efficiency of the radial pre-swirl system, with negligible impact on temperature increment. The optimized model exhibited a 16.93% higher pressure ratio and 1.6% higher temperature ratio than the baseline model. This improvement can be attributed to enhancements in the flow field and reductions in local losses.

1. INTRODUCTION

Improvements in the thermal cycle efficiency of aviation engines are typically associated with an increase in the gas temperature in front of the turbine. This poses a challenge for the thermal protection of turbine blades and disks (Ma et al., 2022; Unnikrishnan & Yang 2022). Ceramic-based barrier coatings have shorter lifespans under high pressures and temperatures (Zhang et al., 2016a). Hoseinzadeh & Heyns (2020) reported that most metallic materials undergo fatigue and creep under critical operating conditions. Furthermore, Ghasemi et al. (2022) analyzed the heat transfer characteristics of functionally graded cylindrical materials, revealing the stress and strain of such materials when exposed to high temperatures. This adverse effect is often eliminated using a radial pre-swirl system to supply a cooling airflow to the first-stage turbine. The airflow in a radial pre-swirl system requires sufficient pressure to achieve sufficient film and impingement cooling to combat blade erosion by high-temperature and high-pressure gases.

The main aim of this study was to optimize the radial pre-swirl system to enhance its supply pressure.

Currently, three main types of pre-swirl systems exist: radial (Zhang et al., 2016b), axial (Lee et al., 2018), and cover plate (Gong et al., 2022). Pre-swirl nozzles, receiver holes, co-rotating cavities, and air supply holes are the most common components in these systems. Figure 1 shows a radial pre-swirl system inside an aircraft engine. The airflow is first extracted from the back cavity of the high-pressure compressor and then sent to the receiver holes through the pre-swirl nozzles. Finally, it flows radially outwards to the air supply holes through a co-rotating cavity. Owing to the stator–rotor interface and acceleration of air, the region of the pre-swirl nozzles and receiver holes has a significant pressure drop, which reduces the quality of the airflow (Liao et al., 2014; Soghe et al., 2018; Liu et al., 2021). However, Shen & Wang (2022) indicated that a co-rotating cavity with radial outflow can increase the pressure of the airflow. Note that the presence of stators, rotors, and multiple components
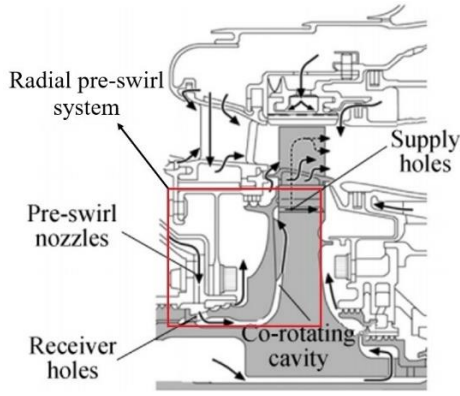
Fig. 1 Schematic of the radial pre-swirl system

poses significant challenges to the optimization design of radial pre-swirl systems.

The number of components must be minimized to reduce the optimization cost of the system. From a spatial perspective, a strong coupling relationship inevitably exists between adjacent components. The efficacy of the co-rotating cavity is primarily affected by the rotational speed, flow rate, and swirl ratio (the ratio of the local absolute tangential velocity to the rotational velocity of the rotating cavity) at the inlet, whereas the latter is primarily influenced by the receiver holes (Owen et al., 1985; Farthing & Owen 1988). In addition, the impact of the pre-swirl nozzles on the co-rotating cavity is small. Moreover, the pressure at the supply holes is closely associated with the local swirl ratio, which is influenced by the swirl ratio at the empty co-rotating cavity inlet (Luo et al., 2014; Hu et al., 2023). To maximize airflow pressure, a set of impellers is positioned within the co-rotating cavity. During this time, the pressure at the supply holes is primarily influenced by the geometric parameters of the impeller (Shen & Wang 2022). In engineering applications, the turbine disk cavity is designed before the radial pre-swirl system; therefore, the geometric parameters of the co-rotating cavity are fixed. Furthermore, the impeller design depends on the inlet swirl ratio and operating conditions. In this study, pre-swirl nozzles and receiver holes were selected as the objects of coordinated optimization.

The temperature of the airflow from the radial pre-swirl system is an important parameter for turbine disks. Zhang & Ding (2012) noted that the instability of the parameters may result in turbine disk fracture. To improve the cooling performance of the system, researchers have conducted a series of optimization studies on the geometric parameters of the pre-swirl nozzle, receiver holes, and supply (Lee et al., 2020, 2021; Kong et al., 2022). Xia et al. (2020) proposed a double-row nozzle to enhance heat transfer on the disk surface. Tang et al. (2022) and Cao et al. (2022) established models to predict the conjugate cavity heat flux density using Bayesian algorithms. However, the pressure performance of radial pre-swirl systems was hardly addressed in these studies.

Overall, previous studies focused on the temperature drop and heat transfer within the pre-swirl system, whereas investigations of the pressure performance of the entire system are lacking. A low-pressure airflow makes it

difficult to satisfy the cooling requirements of turbine rotor blades (Unnikrishnan & Yang 2022). Therefore, in this study, a collaborative design between the pre-swirl nozzles and receiver holes was implemented. Currently, data-driven approaches are widely used to optimize the design of various components (Sun et al., 2023; Xu et al., 2020; Musthafa & Ghosh 2022). In this study, an artificial neural network (ANN) was used to train data from numerical simulations to form a surrogate model, and a particle swarm optimization (PSO) algorithm was used to obtain optimized geometric parameters within the design scope.

The remainder of this paper is organized as follows. In the second section, the computational procedure, including models and methods, is introduced. Design parameters and methods are introduced in the third section. The fourth section examines the training of the surrogate model and presents a comparison between the models before and after optimization. The main conclusions of this study are presented in the fifth section.

2. COMPUTATIONAL PROCEDURE

2.1 Model and Boundary Conditions

Multiple numerical simulations were performed using ANSYS CFX based on the Reynolds-averaged Navier–Stokes (RANS) equations as follows:

$$\rho \bar{u}_j \frac{\partial \bar{u}_i}{\partial x_j} = \rho \bar{f}_i +$$

$$\frac{\partial}{\partial x_j} \left[-\bar{p}\delta_{ij} + \mu \left(\frac{\partial \bar{u}_i}{\partial x_j} + \frac{\partial \bar{u}_j}{\partial x_i} \right) - \rho \overline{u_i' u_j'} \right] \quad (1)$$

where ρ is the density of the fluid, $\bar{u}$ is the time-averaged component of the velocity, u' is the fluctuating component of the velocity, x is the position, $\bar{f}_i$ is the time-averaged external forces, and $\bar{p}$ is the time-averaged pressure.

During the computational procedure, the model was appropriately simplified and the grate seal structure was ignored. The calculation model was divided into two fluid domains based on practical engineering scenarios. The first domain is the static domain comprising the inlet and pre-swirl nozzles. In this region, the airflow completes the pre-swirl process and generates a circumferential velocity. The second domain is the rotating domain, which is primarily composed of receiver holes, a co-rotating cavity, and supply holes, in which the airflow velocity changes from axial to radial. The middle section of the pre-swirl cavity serves as an interface between the stationary and rotating domains of the calculation model. To save computational resources, we selected 1/6 of the periodicity of the original physical model for the computational model, as shown in Fig. 2(a). The axial angle Γ_r, tangential angle θ_r of the receiver holes, and tangential angle θ_n of the pre-swirl nozzles were set as variable geometric parameters. Their values for the baseline model were set to 0°, 0°, and 15°, respectively. The tangential angle of the pre-swirl nozzles is shown in Fig. 2(b), whereas the axial and tangential angles of the receiver holes are shown in Fig. 2(c).
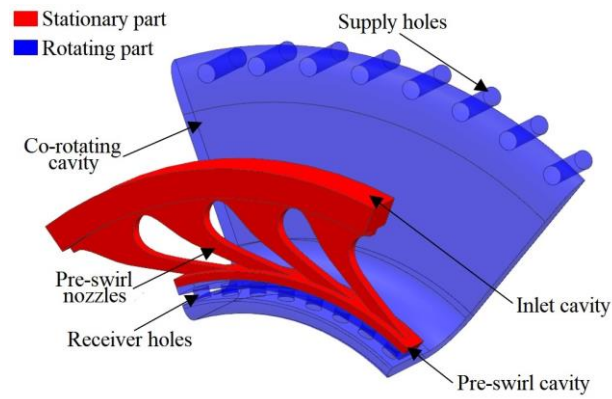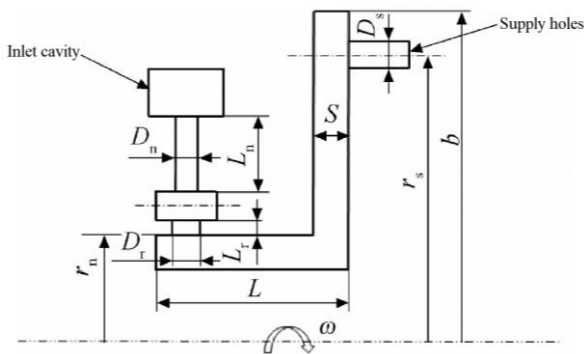
(a) Calculation model
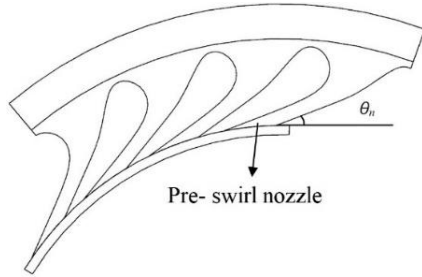
(b) Tangential angle of the pre-swirl nozzles
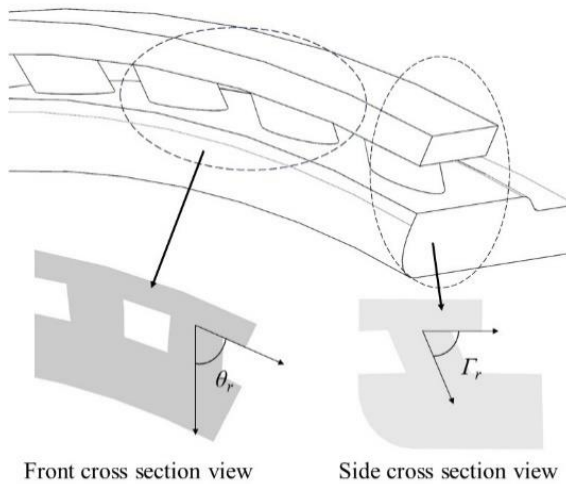
(c) Axial and tangential angles of receiver holes

(d) Geometric parameters of the baseline model

Fig. 2 Structural parameters of the radial pre-swirl system

The geometric parameters of the baseline model are marked in Fig. 2(d) and simplified using the dimensionless representation method based on the radial height r_s where the air supply holes are located. The specific values are listed in Table 1.

Table 1 Dimensionless geometric parameters

Dimensionless geometric parameters	Value
D_n/r_s	0.017
L_n/r_s	0.016
S/r_s	0.049
b/r_s	1.072
L_r/r_s	0.025
D_r/r_s	0.039
D_s/r_s	0.025
L/r_s	0.358

In this study, a compressible ideal gas was used as the working fluid, and its properties were adjusted based on ideal gas properties (Kim et al., 2016). The rotational speed in the rotating region was set at 18000 rpm. Because the static and rotating domains exist simultaneously, a significant circumferential velocity distribution was observed at the outlet of the pre-swirl nozzle. The frozen rotor method was adopted to set the interface on the coincident surfaces of the two domains, and a general grid interface (GGI) was used for grid connection. The periodic surface of the calculation model was set as the rotational periodic boundary condition. The total pressure of the incoming flow at the inlet was specified as 1.3515 MPa and the static temperature was set to 703 K. After the inlet boundary conditions with varying turbulence intensities and comparing the outcomes was evaluated, we determined that the impact of these variations could be ignored. Therefore, the turbulence intensity was fixed at 5%. To avoid interference from unrelated variables while investigating the supercharging effect of the radial pre-swirl system, we constrained the outlet to a fixed mass flow rate of 0.1 kg/s. All the walls in the calculation model were set as adiabatic and no-slip. A summary of the boundary and operating conditions used during the validation process is presented in Tables 2 and 3.

2.2 Grid and Independence Verification

As shown in Fig. 3, ANSYS Meshing was used to grid the computational model. An unstructured mesh was used in the two fluid domains and the element size was set to 1 mm. The mesh was locally refined at the pre-swirl

Table 2 Boundary conditions

Inlet		Outlet	Rotate velocity of rotating part (rev/min)
Total pressure (MPa)	Static temperature (K)	Mass flow rate (kg/s)	
1.3515	703	0.1	18000

Table 3 Operating condition variation range

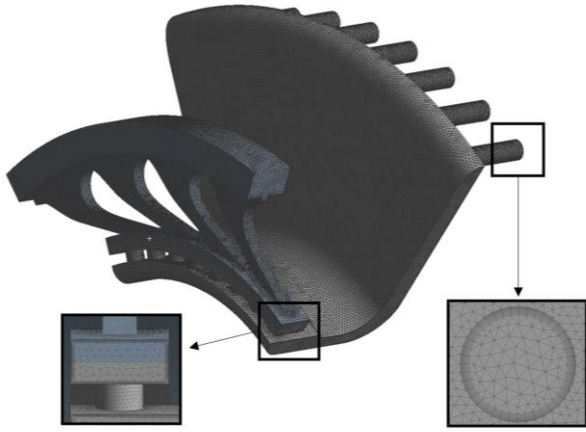| Mass flow rate (kg/s)	Rotating velocity (rev/min)
0.0917–0.1028	9000–21000

Fig. 3 Schematic diagram of computational domains unstructured mesh

nozzles, receiver, and supply holes, such that the size of the surface elements at these locations was set to 0.5 mm. Inflation was established on all walls, except for the periodic surfaces. Using a previous study (Zhang et al., 2020) as a reference, under similar physical models and working conditions, we controlled the y-plus value near the wall within the range of 30–150 to ensure the reliability of the calculation results.

Grids of 700000–3900000 elements were selected to verify grid independence. Figure 4 shows the variation trend of the pressure ratio Π^* (the ratio of the relative total pressure at the outlet of the radial pre-swirl system to that at the inlet) of the radial pre-swirl system with respect to the grid number under the specified boundary conditions above. For a grid number below 3000000, we observed that the total pressure ratio increased steadily with an increase in grid number. Conversely, when the grid number exceeded 3100000, the rate of change in the total pressure ratio was less than 0.1%. Consequently, to guarantee the accuracy and reliability of the computational outcomes and to conserve computational resources, we used a grid with 3100000 cells for all subsequent calculation models incorporating different geometric parameters. This selection encompassed grids of approximately 1000000 elements in the stationary domain and approximately 2100000 in the rotating domain.
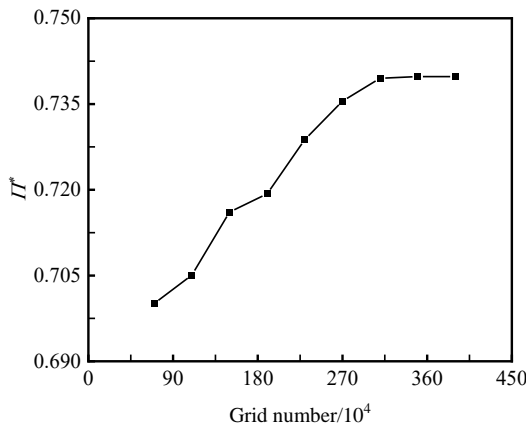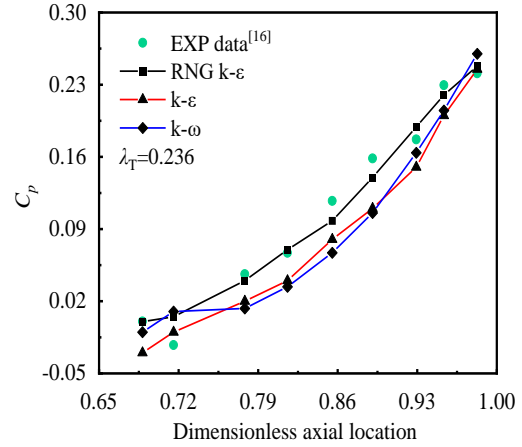

Fig. 4 Grid independence verification

Fig. 5 Turbulence model verification

2.3 Turbulence Model Verification

To verify the reliability of the calculation results, we used experimental data from Kong et al. (2022) to validate the most appropriate turbulence model. An additional computational model was established with respect to the details of their computational model, and it was applied in the test. The boundary conditions of the test were set the same as those used in their research. The mesh and simulation methods applied in the test were consistent with those used in this study. We define the static pressure coefficient (C_p) as follows:

$$C_p = \frac{p - p_1}{\frac{1}{2}\rho\omega^2 r_1^2} \tag{2}$$

where p_1 is the inlet static pressure of the computational model, ω is the angular velocity, and r_1 is the radial inlet location. The simulation result of the test was used to perform a comparison with the experimental result, as shown in Fig. 5. The turbulent flow parameter $\lambda_T = C_w \cdot Re_\phi^{-0.8}$, C_w is dimensionless mass flow rate, and Re_ϕ is the rotational Reynolds number. The dimensionless axial location is equal to the actual axial location divided by the total axial length. The simulation result of the RNG k-ε turbulence model and experimental data had the best agreement. This was because the RNG model considers the effect of vortices on turbulent flow, thereby enhancing the accuracy of vortex flow, and providing an analytical formula for the turbulent Prandtl number, which makes the fitting for turbulent flow more accurate (Han & Reitz 1995). Thus, the RNG k-ε turbulence model was used for all subsequent calculations.

The transport equations of the RNG k-ε turbulence model are expressed as follows:

$$\frac{\partial}{\partial t}(\rho k) + \frac{\partial}{\partial x_i}(\rho k u_i) =$$
$$\frac{\partial}{\partial x_j}[\alpha_k \mu_{eff} \frac{\partial k}{\partial x_j}] + G_k + G_b - \rho\varepsilon - Y_M + S_k \tag{3}$$

$$\frac{\partial}{\partial t}(\rho\varepsilon) + \frac{\partial}{\partial x_i}(\rho\varepsilon u_i)$$
$$= \frac{\partial}{\partial x_j}\left[\alpha_s \mu_{eff}\frac{\partial\xi}{\partial x_j}\right]$$
$$+ C_{1\varepsilon}\frac{\xi}{k}(G_k + C_{3e}G_b) \qquad (4)$$
$$- C_{2s}\rho\frac{\xi^2}{k} - R_\varepsilon + S_\varepsilon$$

where k is the kinetic energy, ε is the dissipation rate of k, G_k represents the generation of turbulence kinetic energy due to the mean velocity gradients, G_b is the generation of turbulence kinetic energy due to buoyancy, Y_M is the contribution of the fluctuating dilatation in compressible turbulence to the overall dissipation rate, α_k and α_s are the inverse effective Prandtl numbers for k and ε, respectively, and S_k and S_ε are source terms.

3. GEOMETRIC PARAMETERS DESIGN AND OPTIMIZATION METHODOLOGY

3.1 Geometric Parameters Design and Optimization Methodology

As previously stated, this study focused on three variable geometric parameters: the tangential angle of the pre-swirl nozzles, the axial angle, and the tangential angle of the receiver holes. The computational procedure employed a wide range of parameter variations to achieve a significant improvement in the pressure-boosting performance. To ensure uniform changes in all three parameters and maintain the overall aerodynamic and structural design rationality, we changed the scope of all the variable geometry parameters by 30°.

For the baseline model, the initial tangential angle of the pre-swirl nozzle was set to 15°, and the initial angles of the other two parameters were set to 0°. During the computational procedure, the parameters underwent seven changes with each change increasing by 5°. The final values of the three geometric parameters were determined to be 45° for the tangential angle of the pre-swirl nozzles and 30° for both the axial and tangential angles of the receiver holes. The variations in structural parameters are listed in Table 4.

Figure 6 shows a flowchart of the optimization procedure, the specific steps of optimization of which are listed below:

1. Determine the geometric parameters that would be adopted in the subsequent steps to achieve the optimization effect.

Table 4 Geometric parameter variation range

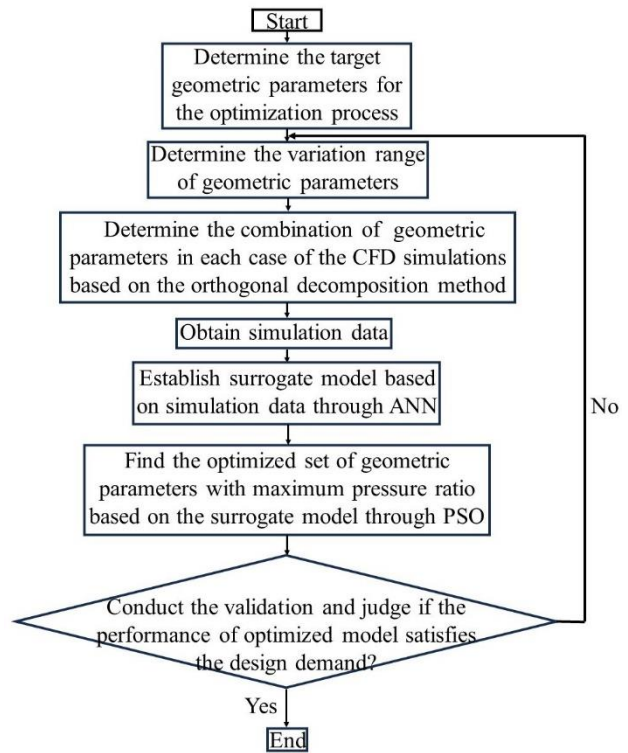| Geometric parameters	Range of value (°)
Tangential angle of the pre-swirl nozzles	15–45
Tangential angle of the receiver holes	0–30
Axial angle of the receiver holes	0–30

Fig. 6 Flow chart of the optimization procedure

2. Determine the variation range for each geometric parameter mentioned in step 1.

3. Determine the combination of values to be used for each geometric parameter during the simulation process based on the orthogonal decomposition method, and acquire the simulation data for each combination.

4. Establish a surrogate model that demonstrates the relationship between geometric parameters and pressure ratio using an ANN. In addition, use the PSO algorithm to locate a combination of geometric parameters that provides the highest pressure ratio within the variation range.

5. Determine whether the optimized result can satisfy the demand, which consists of performing at least 10% better than the baseline model under the operating conditions and having at least two geometric parameters that do not fall within the variation range boundary. If the demand is satisfied, then optimization is performed; otherwise, return to step 2.

3.2 Artificial Neural Network

A neural network is a machine learning methodology inspired by the signaling process between neurons in the human brain. This technique is particularly well-suited for analyzing nonlinear relationships (Jain et al., 1996); hence, it was employed in this investigation to determine the correlation between the geometric and performance parameters of a radial pre-swirl system. The neural-network fitting process used in this study was implemented using Python. The process of training an ANN is shown in Fig. 7, where the three input quantities
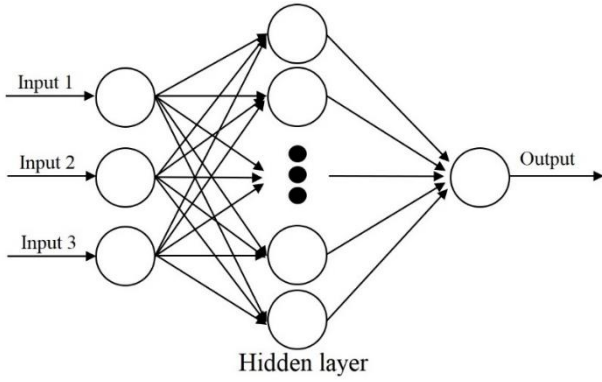
Fig. 7 Schematic of an ANN

Fig. 8 Chart flow of the PSO algorithm

are the tangential angle of the pre-swirl nozzle and the tangential and axial angles of the receiver holes, and the final output quantity is the total pressure ratio.

3.3 PSO Algorithm

The PSO algorithm is a computational technique used to optimize problems by continually attempting to enhance a potential solution based on a predefined measure of quality. The PSO algorithm operates by maintaining a population of candidate solutions called a "swarm." The particles within the swarm are navigated using Eqs. (5) and (6) in the search space (Fernández Martínez et al., 2008):

$$V_i^{k+1} = \omega V_i^k + c_1 r_1 \left(p_i^k - x_i^k \right) + c_2 r_2 \left(p_g^k - x_i^k \right) \qquad (5)$$

$$X_i^{k+1} = X_i^k + V_i^{k+1} \qquad (6)$$

where V is the velocity of the particles, X is the position of the particles, p_i is the best-known position of a specific particle, p_g is the globally best position, c is the learning factor, and ω and r are the pseudorandom numbers in the range from zero to one; ω is a constant called inertia, and r affects c. The superscript for the physical quantity represents the number of time steps. The following second-order vector difference equations are also included in the PSO algorithm for each particle in the swarm (Fernández Martínez et al., 2008) to introduce a new variable $\xi_i^k = x_i^k - o_i^k$, which represents the particles positions in certain iteration, referred to as their oscillation center o_i^k:

$$\xi_i^{k+1} + (c_1 r_1 + c_2 r_2 - \omega - 1)\xi_i^k + \omega \xi_i^{k-1} = \beta(o) \qquad (7)$$

$$\beta(o) = o_i^k - o_i^{k+1} + \omega(o_i^k - o_i^{k-1}) \qquad (8)$$

A flowchart of PSO is shown in Fig. 8. The PSO algorithm employed in this study was implemented in Python. The detailed steps of the PSO algorithm are as follows:

1. Initialize the particles in the swarm randomly to obtain the initial value, which was a random assignment of three variable geometric parameters in this study.

2. Evaluate all particles and determine the global optimum output value.
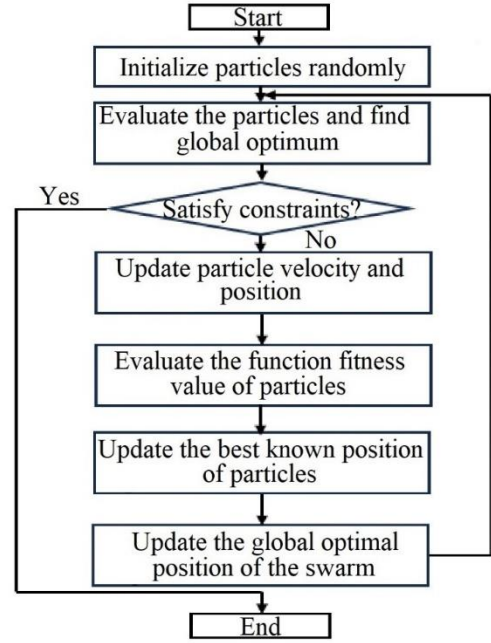
3. Determine whether the optimum value found in step 2 can satisfy the constraint conditions, for instance, the maximum number of iterations. If this is satisfied, the process ends.

4. If the constraints are not satisfied, the particles move. The movements of the particles are influenced by their own best-known positions as well as the best-known positions of the entire swarm. As newly improved positions are discovered, they can guide the movement of the swarm.

5. After the particles move, the fitness value is evaluated, and the best-known and global optimal positions of the particles are updated.

6. Return to step 2.

4. RESULTS AND ANALYSIS

4.1 Surrogate Model

This investigation examined three geometric parameters that were modified seven times. Using the orthogonal decomposition method (Taguchi, 1986), we reduced the total number of necessary calculations from 7^3 to 7^2, resulting in significant computational resource savings. Seven sets of data were used for testing, 35 sets of data were used for training, and another seven sets of data were used to verify the ANN fit results of the ANN fitting. Table 5 provides an overview of the training, testing, and validation datasets used in this study.

The Levenberg–Marquardt method was adopted for the training process (Wilamowski & Irwin 2018), and training performance was measured using the mean square error (MSE). The MSE and regression value (R) of the training, verification, and testing processes are listed in Table 6. The MSE value was less than 1e-3 for the three

Table 5 Training, testing, and validation data

Serial number	Receiver holes tangential angle (°)	Receiver-hole axial angle (°)	Pre-swirl-nozzle tangential angle (°)	Dimensionless total pressure ratio
1	0	0	15	0.7810
2	0	5	25	0.7436
3	0	10	35	0.7762
4	0	15	45	0.7910
5	0	20	20	0.7525
6	0	25	30	0.7584
7	0	30	40	0.7895
8	5	0	45	0.7836
9	5	5	20	0.7481
10	5	10	30	0.7614
11	5	15	40	0.7954
12	5	20	15	0.7584
13	5	25	25	0.7584
14	5	30	35	0.7888
15	10	0	40	0.7954
16	10	5	15	0.7599
17	10	10	25	0.7688
18	10	15	35	0.7954
19	10	20	45	0.8073
20	10	25	20	0.7784
21	10	30	30	0.7762
22	15	0	30	0.7688
23	15	5	40	0.8073
24	15	10	15	0.7784
25	15	15	25	0.7784
26	15	20	35	0.8080
27	15	25	45	0.8142
28	15	30	20	0.7762
29	20	0	25	0.7725
30	20	5	35	0.8124
31	20	10	45	0.8183
32	20	15	20	0.7821
33	20	20	30	0.7902
34	20	25	40	0.8176
35	20	30	15	0.7836
36	25	0	20	0.8013
37	25	5	30	0.8028
38	25	10	40	0.8228
39	25	15	15	0.7932
40	25	20	25	0.7895
41	25	25	35	0.8154
42	25	30	45	0.8339
43	30	0	35	0.8191
44	30	5	45	0.8369
45	30	10	20	0.8028
46	30	15	30	0.8058
47	30	20	40	0.8302
48	30	25	15	0.8065
49	30	30	25	0.7999

processes, and R was greater than 0.80. The fitting results for the neural network are presented in Fig. 9. The difference between the surrogate model and the calculated data was less than 3%. Overall, the fitting results were considered accurate.

A surrogate model established using ANN fitting was Used to construct the fitness function in the PSO. In this study, the maximum number of iterations in the PSO process was 100, and the iteration results are shown in Fig. 10. The result value tended to be stable after the number of iteration steps reached 15 and remained unchanged in the subsequent iterations of approximately 85. We can

Table 6 MSE and R values in the ANN fitting process

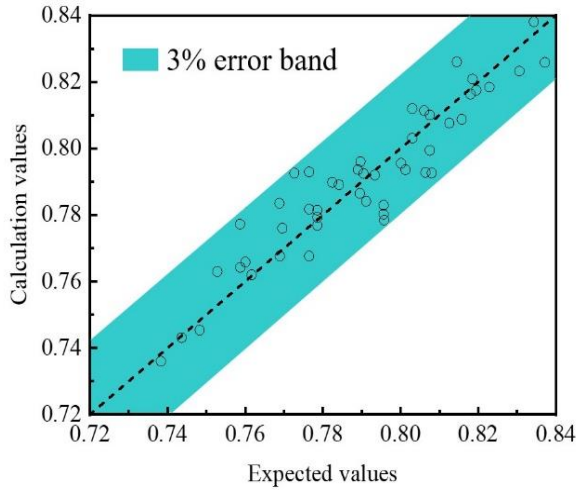| Process	Observed value	MSE	R
Training	35	8.6594e-05	0.9307
Verification	7	3.4876e-05	0.9688
Testing	7	1.2449e-04	0.8049

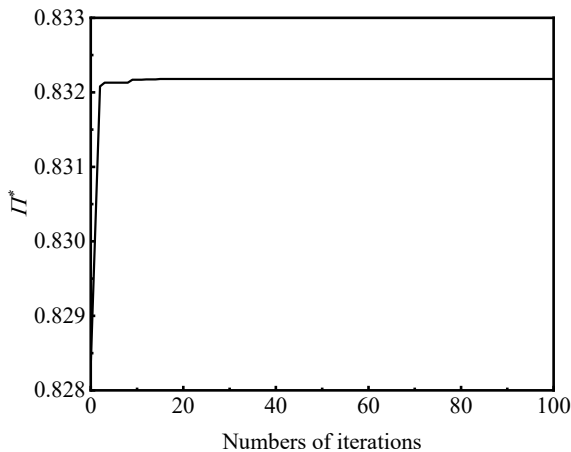**Fig. 9 Surrogate model vs. calculation data.**

Fig. 10 PSO iteration result.

PSO reached a stable state after the iteration process. The highest global historical optimal fitness value (pressure ratio) was 0.8322, which was obtained when the tangential angle of the pre-swirl nozzles was 40.4368°, the axial angle of the receiver holes was 2.0286°, and the tangential angle of the receiver holes was 30°. A four-dimensional data visualization of the three geometric parameters and pressure ratio is shown in Fig. 11. The pressure ratio increased with the tangential angle between the pre-swirl nozzles and receiver holes. This was attributed to the transformation of the swirl ratio in the pre-swirl cavity and at the receiver hole outlet, which improved the flow field and reduced local losses. However, the axial angle of the receiver hole had a less significant effect on the overall radial pre-swirl system, and the change in the pressure ratio was not significant.
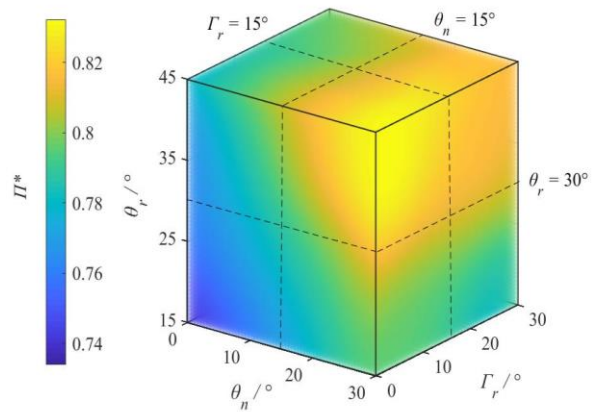
(a) Four-dimensional data visualization
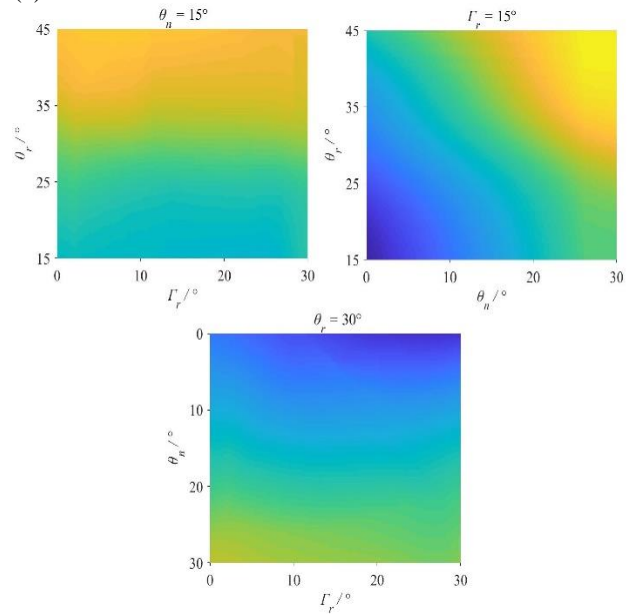

(b) Sections along three directions
Fig. 11 Data visualization of pressure ratio

## 4.2 Flow Resistance of the Radial Pre-Swirl System

Figure 12 shows the streamlines and normalized entropy (local entropy minus inlet entropy) within the tangential and axial portions of both the baseline and optimized models. The pre-swirl nozzle guides the airflow according to its structural design, resulting in the generation of a tangential velocity component, which results in local losses at the junction between the rotating and stationary domains. In the basic model, the receiver hole tangential angle was zero, which caused the boundary layer to shed on the leeward side of the receiver hole and form a stationary vortex at the outlet of the receiver hole. Therefore, significant mixing between the different fluids caused a surge in the local normalized entropy. However, the optimized model had a larger tangential angle for the pre-swirl nozzle and receiver hole, which enhanced the local flow field while minimizing the increase in local entropy. Furthermore, the optimized receiving hole had an axial angle that enabled the airflow to transition smoothly from the radial direction to the axial direction. Overall, compared with the baseline model, the optimized model experienced a 34.65% reduction in the entropy increase.
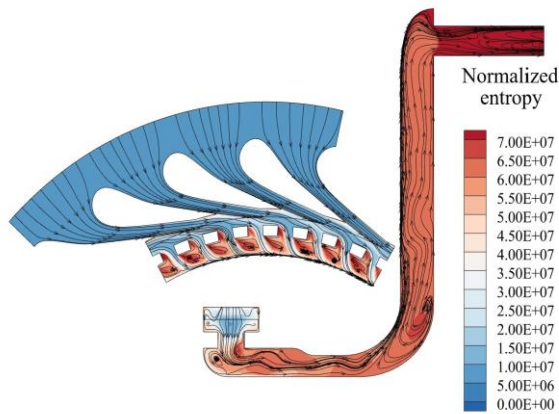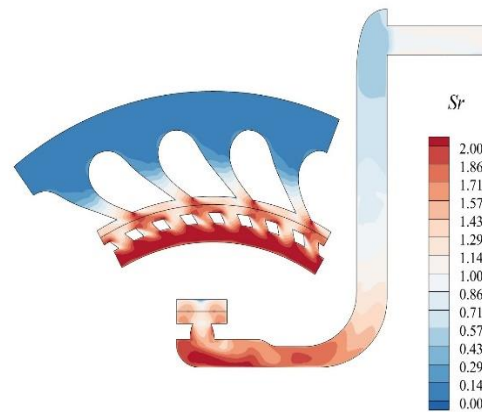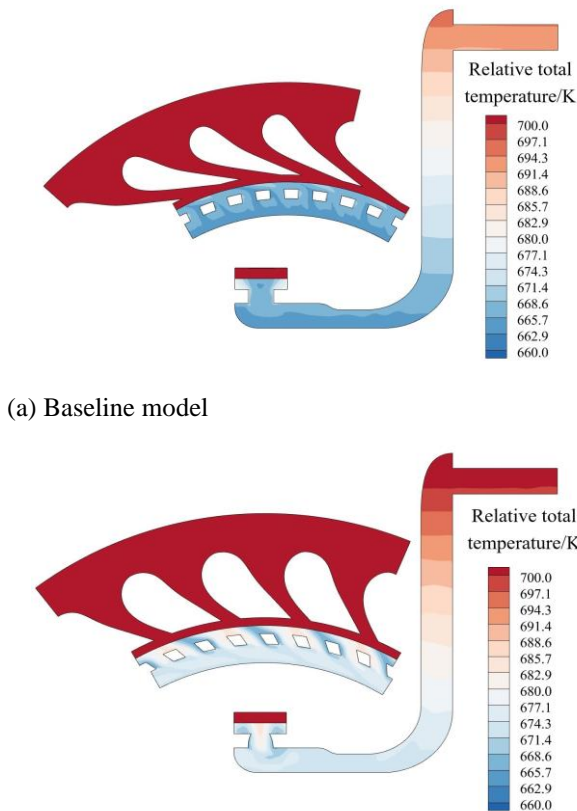
(a) Baseline model
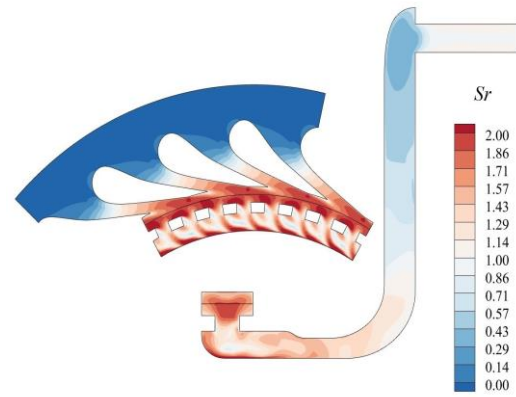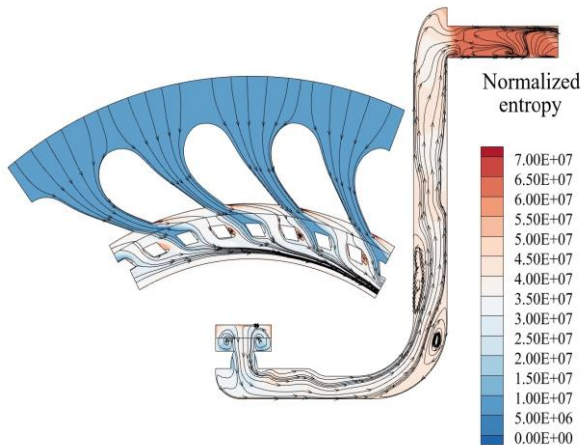
(b) Optimized model

Fig. 12 Streamline-normalized entropy distribution.

(a) Baseline model

(b) Optimized model

Fig. 13 Swirl ratio distribution.

The swirl ratio is commonly used to assess the flow characteristics in a radial pre-swirl system and identify its internal temperature and pressure changes (Owen et al., 1980). Figure 13 shows the distribution of the swirl ratio in the tangential and axial sections for both the baseline and optimized models. Because of the structural features of the pre-swirl nozzles, the airflow was constantly accelerated, producing a rapid increase in the swirl ratio. In the baseline model, the pre-swirl cavity exhibited a high swirl ratio of up to 2.00. However, the presence of receiver holes in the baseline model constrained the development of the swirl ratio, resulting in a sudden increase in the local normalized entropy. The optimized model had a larger tangential angle and pre-swirl nozzles, which reduced the tangential component of the pre-swirl jet. This caused the local swirl ratio to weaken and the swirl ratio at the outlet of the receiver hole to increase to 2.00. Furthermore, the swirl ratio continuously decreased during the radial outflow of air in the co-rotating cavity. At relatively low flow rates, an Ekman layer appeared within the co-rotating cavity, resulting in an increase in the swirl ratio (Owen et al., 1985). However, for engineering purposes, the radial pre-swirl system must have a higher flow rate to meet the cooling demands. Therefore, in this study, the source region filled the co-rotating cavity. It is particularly important to increase the air velocity at the supply holes, resulting in a swirl ratio of up to 1.

Although the objective of this study was to determine the pressure ratio, the drop in temperature was also an essential evaluation indicator. Figure 14 depicts the relative total temperature distributions in the tangential and axial sections of the basic and optimized models. The distribution of the relative total temperature was similar in both models for different geometric parameters. The total relative temperature of the airflow remained unchanged in the stationary domain. However, owing to the movement of the reference frame, the relative total temperature of the pre-swirl cavity suddenly decreased. Because the optimized model had a larger tangential angle for the pre-swirl nozzles, the tangential velocity of the pre-swirl jet was lower, thereby reducing the acceleration effect. Consequently, the optimized model exhibited a lower temperature drop in the pre-swirl cavity and receiver holes than the unaltered baseline model. According to Shen & Wang (2022), the relative total temperature of the airflow remained unchanged in a co-rotating cavity with a radial flow, even when the wall was insulated and wind resistance was not considered. However, in the process of airflow from the low radius to the high radius of the cavity in this study, owing to wind resistance, the relative total temperature of the airflow tended to increase gradually. The relative total temperature at the average mass flow rate of the air supply holes in the optimized model was 1.15% higher than that in the baseline model.

(a) Baseline model

(b) Optimized model

**Fig. 14 Distribution of the relative total temperature.**

Figure 15 shows the pressure ratio distributions for the baseline and optimized models. Because the gas flow was accelerated by the structure in the pre-swirl nozzles and had a high flow loss in the receiver holes, the gas flow exhibited an observable pressure drop at these two locations. However, compared with the baseline model, the optimized model encompassed a greater tangential angle for both the pre-swirl and receiver holes. This culminated in a lower magnitude of the jet tangential velocity component at the pre-swirl nozzle outlet in the optimized model, ultimately reducing the flow loss at the receiver holes. Compared with the baseline model, the relative total pressure drops of the pre-swirl nozzles and receiver hole area at the design point decreased by 18.93% and 46.97%, respectively, as shown in Fig. 16(b). Further observations indicated that the pressure ratio remained relatively unchanged along the axial direction at the outlet of the receiver holes in both models, suggesting that the axial angle of the receiver holes had a minimal impact on the pressure ratio, which was consistent with the optimization outcomes of the surrogate model. Because the inlet swirl ratio was greater in the optimized model, the centrifugal pressure rise for the co-rotating cavity increased by 30.88% compared to the baseline model (Fig. 16(b)). The overall pressure ratio of the optimized model after calculation was 0.8391, which was essentially the same as the predicted value of the surrogate model, resulting in a 13.68% higher ratio than that of the baseline model.
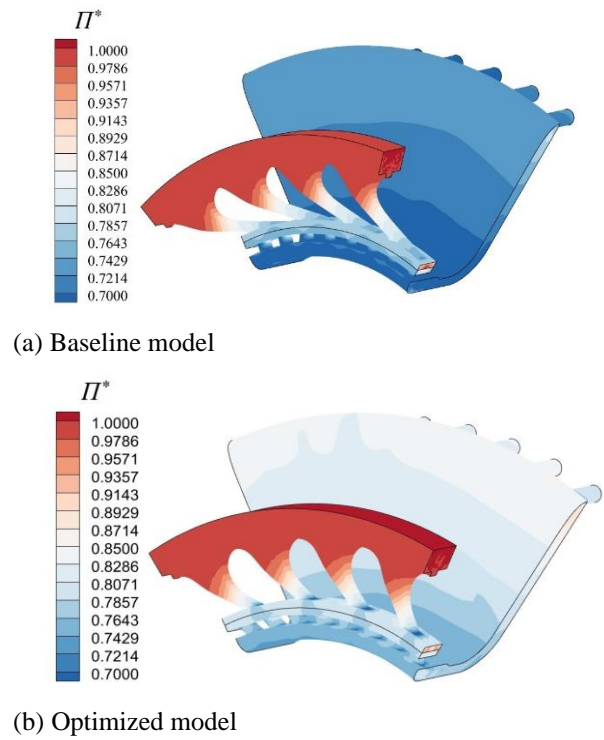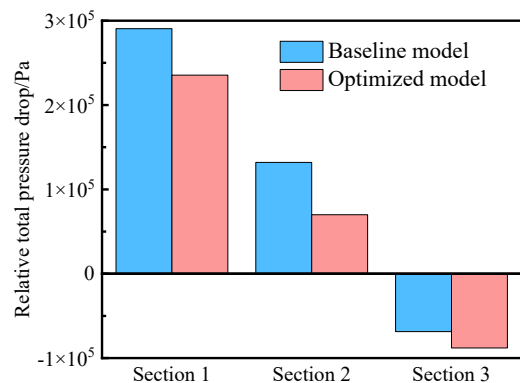

(a) Baseline model

(b) Optimized model

Fig. 15 Relative total pressure distribution.
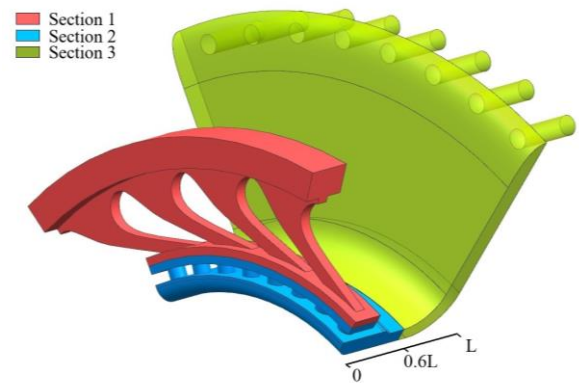
(a) Section location

(b) Pressure drop histogram

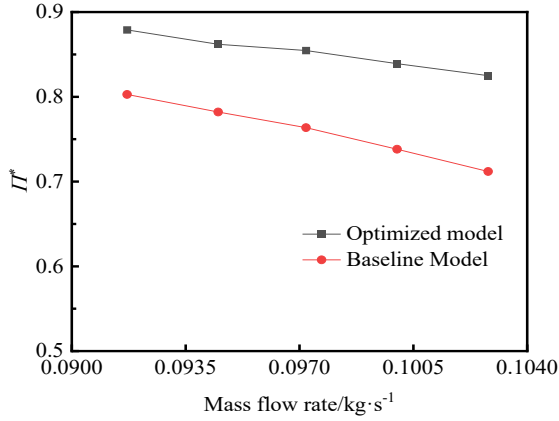**Fig. 16 Relative total pressure drop in each section**

Fig. 17 Pressure ratio at different mass flow rates

Fig. 18 Pressure ratio at different rotating velocities

4.3 Performance Validation of the Optimized Radial Pre-Swirl System

Calculations were performed at different operating points to validate that the optimized radial pre-swirl system exhibited good performance in addition to the design-point operating conditions.

Figure 17 shows the variation in the pressure ratio between the baseline and optimized models at different mass flow rates. The pressure ratios of both models decreased as the flow rate increased. In the pre-swirl cavity and receiver holes, a strong pre-swirl jet caused a high local flow loss and an increase in entropy. As the swirl ratio was assumed to remain constant over a short axial length, the swirl ratio at the entry of the co-rotating cavity was the same as that at the exit of the receiver holes. For a co-rotating cavity, a high inlet swirl ratio can increase the pressure rise at a high mass-flow rate (Owen et al., 1980). However, because the baseline model enabled a tangential hole angle of 0°, the corresponding inlet swirl ratio remained constant at 1. In the optimized model, the swirl ratio of the co-rotating cavity inlet increased as the mass flow rate increased. Furthermore, the optimized model exhibited an increase in the swirl ratio at the inlet of the air supply holes, resulting in a smaller relative velocity and thus lower local losses than the basic model at the same flow rate. Therefore, the optimized model had a smaller pressure ratio decrease rate than the baseline model. On average, the pressure ratio of the optimized model was 12.31% higher than that of the baseline model owing to the reduced local losses and increased boosting efficiency in the rotating cavity.

Figure 18 shows the pressure ratios of the baseline and optimized models at different rotating velocities. Owing to the increase in the rotating speed, the pre-swirl ratio (swirl ratio in the pre-swirl cavity) of the airflow decreased; therefore, the local loss in the pre-swirl cavity and receiver holes decreased. In the co-rotating cavity, the pressure rise satisfies Eqs. (9) and (10) (Firouzian et al., 1986):

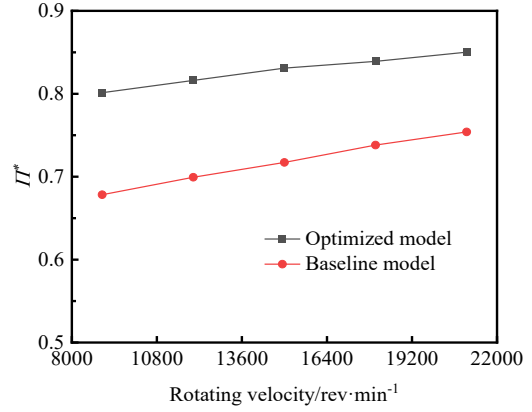$$\Delta p = \int_{r_1}^{r_2} \rho r \omega^2 Sr_c^2 \, dr \tag{9}$$

$$Sr_c = c \frac{x_n^2}{x^2} \tag{10}$$

where Sr_c is the local swirl ratio in the co-rotating cavity, $x_n = \frac{r_n}{b}$, $x = \frac{r}{b}$ is the dimensionless height along the radial direction, c is the swirl ratio of the co-rotating cavity inlet, which equals the swirl ratio of the receiver hole outlet, and ω is the rotational angular velocity.

In a co-rotating cavity with a radial outflow, a small swirl ratio represents a low absolute tangential velocity, and a low Mach number produces a limited pressure rise; therefore, the density is considered to be constant. The expression for the swirl ratio at the outlet of the receiving hole is given by

$$c = \frac{\frac{\dot{m}}{\rho A_r} sin\theta_r}{\omega r_n} + 1 \tag{11}$$

where A_r is the effective cross-sectional area of the receiver holes, and $\dot{m}$ is the mass flow rate. Combining Eqs. (9) to (11), we obtain:

$$\Delta p = \left(\frac{\frac{\dot{m}}{\rho A_r} sin\theta_r}{r_n} + \omega \right)^2 \int_{r_1}^{r_2} \rho \frac{a^4}{r^3} \, dr \tag{12}$$

When the rotational speed increases, the pressure in the co-rotating cavity increases. Therefore, the pressure ratio of the radial pre-swirl system increases with the rotational speed. Additionally, the optimized model had a higher corotating cavity inlet swirl ratio and smaller local loss, resulting in a consistently greater pressure ratio than the baseline model. Note that, compared with the baseline model, the increase rate of the pressure ratio decreased with an increase in the speed of the optimized model. Generally, at the entrance of the receiving hole, the local loss was proportional to the square of the relative velocity, as shown in Eq. (13).

$$\Delta p \propto v_r^2 \tag{13}$$

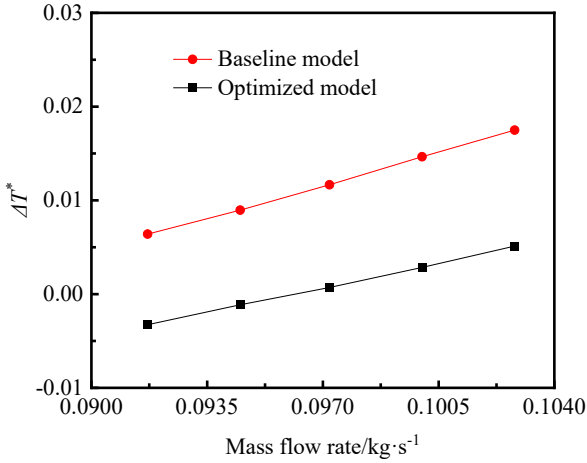substituting the definition of the swirl ratio into Eq. (13), we obtain

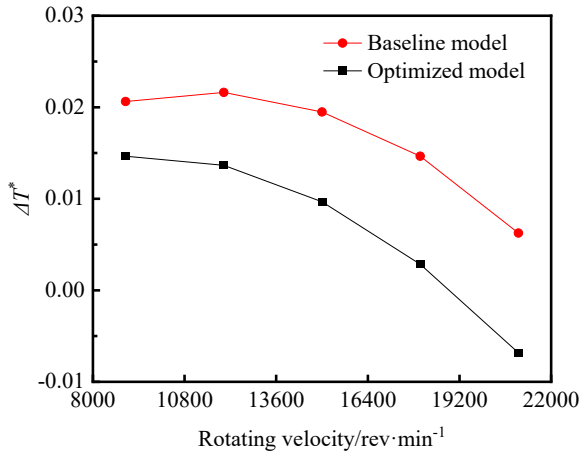**Fig. 19 Temperature coefficient at different mass flow rates.**

Fig. 20 Temperature coefficient under different rotating velocities.

$$\Delta p \propto \omega^2 r^2 (Sr - 1)^2 \qquad (14)$$

Because the baseline model had a larger swirl ratio in the pre-swirl cavity, it gained a larger relative tangential velocity change when the swirl ratio changed by the same amount as in the optimized model. In other words, the local loss of the baseline model was more sensitive to changes in the relative velocity. Even when the swirl ratio of the optimized model was greater than 1 at the entrance of the pre-swirl cavity, it had a greater efficiency in pressurizing air as the rotating velocity in the pre-swirl cavity increased. However, the effect of the entire radial pre-swirl system on pressure boosting was still lower than the positive effect of the reduced local losses at the pre-swirl nozzles and receiver holes. Therefore, the optimized model exhibited a softer boosting tendency with increasing rotational velocity, as shown in Fig. 18.

Figures 19 and 20 show the effects of the mass flow and rotating velocity, respectively, on the temperature coefficient in the two models. Because the optimized model had a weaker pre-swirl jet than the baseline model, the temperature drop was lower. As the mass flow rate

increased, the tangential component of the pre-swirl jet from the pre-swirl nozzles increased, the swirl ratio in the pre-swirl cavity increased, and the temperature drop in the system gradually increased. As the rotating velocity increased, the swirl ratio of the pre-swirl cavity decreased, the pre-swirl jet flow weakened, and the local temperature drop decreased. In the rotating cavity, as the relative speed increased, the temperature increase caused by the flow resistance increased. Therefore, the temperature drop coefficients in both the models decreased.

5. CONCLUSION

This study used an ANN to establish a surrogate model of the radial pre-swirl system, which was then used in conjunction with the PSO algorithm to obtain the optimized geometric parameters within the design scope. Furthermore, the flow pressure and temperature of the optimized model were investigated and its performance was evaluated. The following are the key findings of this study:

1. The tangential angle of the pre-swirl nozzles in the optimized model was determined to be 40.4368°, whereas the axial angle of the receiver hole was 2.0286° and the tangential angle was 30°, which were larger than the same angles in the baseline model. By increasing the tangential angle of the pre-swirl nozzles, the swirl ratio of the pre-swirl cavity was reduced to 1, thereby significantly decreasing the local loss. Similarly, the resulting tangential angle of the receiver hole enhanced the pressurization of the co-rotating cavity by increasing the inlet swirl ratio and reducing the local loss of the air supply holes.

2. The supercharging performance of the optimized model was significantly improved, and no rapid increase in temperature was observed. The optimized model experienced less local loss and a stronger pressurization effect in the co-rotating cavity, resulting in a high pressure ratio of 0.8391. This ratio remained consistent with the PSO prediction results and was 13.68% higher than that of the baseline model. Additionally, the relative total temperature of the optimized model surpassed that of the baseline model by only 1.15%.

3. The pressure ratios of both the baseline and optimized models exhibited a descending pattern with increasing flow rates. This phenomenon was attributed to the intensified jet strength at the outlet of the pre-swirl nozzles, which led to a subsequent increase in local loss and, consequently, a decrease in pressure ratios. However, owing to the higher inlet swirl ratio in the optimized model compared with the baseline model, the enhanced centrifugal supercharging mitigated the rate of the pressure ratio drop in the optimized model.

4. Both the baseline and optimized models exhibited an increasing trend in the pressure ratios as the rotating velocity increased. Increasing the rotation velocity caused a decrease in the swirl ratio and relative tangential velocity in the pre-swirl cavity, resulting in a decrease in the local loss. Conversely, a higher rotation velocity strengthened the effect of centrifugal supercharging in the co-rotating cavity. However, because

the baseline model had a higher pre-swirl ratio, the reduction in local loss caused by the velocity increase was more noticeable, resulting in a higher rate of pressure ratio increase compared with the optimized model.

Generally, the airflow pressure in the radial pre-swirl system underwent a significant increase, whereas no significant change occurred in the temperature. These results demonstrated that the optimized model has engineering value. However, note that the cavity pressurization performance would be affected by various structures installed in the co-rotating cavity. As research on the structural impact of supercharging is lacking, future studies should consider a wider variation range of current geometric parameters and other typical structures applied in practical engineering cases. Furthermore, physical experiments should be conducted for a more accurate verification of the optimization results.

ACKNOWLEDGEMENTS

CONFLICT OF INTEREST

The authors declare no conflict of interest.

AUTHORS CONTRIBUTION

Difei Wang: Conceptualization, methodology, software, validation, formal analysis, investigation, resources, data curation, writing—original draft preparation, writing—review and editing, visualization; **Chenxi Qiu**: Conceptualization, methodology, software, validation, formal analysis, investigation, data curation; **Chi Song**: software, validation, formal analysis, investigation, resources, data curation, writing—original draft preparation, writing—review and editing, visualization; **Yifan Xu**: formal analysis, investigation; **Weicheng Wang**: formal analysis, investigation; **Platonov Ivan Mihailovich**: Conceptualization, methodology, validation, investigation, writing—review and editing.

REFERENCES

Cao, N., Luo, X., & Tang, H. (2022). A Bayesian model to solve a two-dimensional inverse heat transfer problem of gas turbine discs. *Applied Thermal Engineering*, *214*, 118762. https://doi.org/10.1016/j.applthermaleng.2022.118762

Da Soghe, R., Bianchini, C., & D'Errico, J. (2018). Numerical characterization of flow and heat transfer in preswirl systems. *Journal of Engineering for Gas Turbines and Power*, *140*(7), 071901. https://doi.org/10.1115/1.4038618

Farthing, P. R., & Owen, J. M. (1988). The effect of disk geometry on heat transfer in a rotating cavity with a radial outflow of fluid. *Journal of Engineering for Gas Turbines and Power*, *110*(1), 70-77.

https://doi.org/10.1115/1.3240089

Fernández Martínez, J. L., & García Gonzalo, E. (2008). The generalized PSO: A new door to PSO evolution. *Journal of Artificial Evolution and Applications*, 2008. https://doi.org/10.1155/2008/861275

Firouzian, M., Owen, J. M., Pincombe, J. R., & Rogers, R. H. (1986). Flow and heat transfer in a rotating cylindrical cavity with a radial inflow of fluid: Part 2: Velocity, pressure and heat transfer measurements. *International journal of Heat and Fluid Flow*, *7*(1), 21-27. https://doi.org/10.1016/0142-727x(86)90037-8

Ghasemi, M. H., Hoseinzadeh, S., & Memon, S. (2022). A dual-phase-lag (DPL) transient non-Fourier heat transfer analysis of functional graded cylindrical material under axial heat flux. *International Communications in Heat and Mass Transfer*, *131*, 105858. https://doi.org/10.1016/j.icheatmasstransfer.2021.105858

Gong, W., Liu, G., Wang, J., Wang, F., Lin, A., & Wang, Z. (2022). Aerodynamic and thermodynamic analysis of an aero-engine pre-swirl system based on structure design and performance improvement. *Aerospace Science and Technology*, *123*, 107466. https://doi.org/10.1016/j.ast.2022.107466

Han, Z., & Reitz, R. D. (1995). Turbulence modeling of internal combustion engines using RNG κ-ε models. *Combustion Science and Technology*, *106*(4-6), 267-295. https://doi.org/10.1080/00102209508907782

Hoseinzadeh, S., & Heyns, P. S. (2020). Thermo-structural fatigue and lifetime analysis of a heat exchanger as a feedwater heater in power plant. *Engineering Failure Analysis*, *113*, 104548. https://doi.org/10.1016/j.engfailanal.2020.104548

Hu, B., Yao, Y., Wang, M., Wang, C., & Liu, Y. (2023). Flow and performance of the disk cavity of a marine gas turbine at varying nozzle pressure and low rotation speeds: a numerical investigation. *Machines*, *11*(1), 68. https://doi.org10.3390/machines11010068

Jain, A. K., Mao, J., & Mohiuddin, K. M. (1996). Artificial neural networks: A tutorial. *Computer*, *29*(3), 31-44. https://doi.org/10.1109/2.485891

Kim, J., Kang, Y. S., Kim, D., Lee, J., Cha, B. J., & Cho, J. (2016). Optimization of a high pressure turbine blade tip cavity with conjugate heat transfer analysis. *Journal of Mechanical Science and Technology*, *30*, 5529-5538. https://doi.org/10.1007/s12206-016-1121-6

Kong, X., Huang, T., Liu, Y., Chen, H., & Lu, H. (2022). Effects of pre-swirl radius on cooling performance of a rotor-stator pre-swirl system in gas turbine engines. *Case Studies in Thermal Engineering*, *37*,

102250. https://doi.org/10.1016/j.csite.2022.102250

Lee, H., Lee, J., Kim, S., Cho, J., & Kim, D. (2018, June). *Pre-swirl system design including inlet duct shape by using CFD analysis*. Turbo Expo: Power for Land, Sea, and Air (Vol. 51098, p. V05BT15A029). American Society of Mechanical Engineers. https://doi.org/10.1115/GT2018-76323

Lee, J., Lee, H., Kim, D., & Cho, J. (2020). The effect of rotating receiver hole shape on a gas turbine pre-swirl system. *Journal of Mechanical Science and Technology*, *34*, 2179-2187. https://doi.org/10.1007/s12206-020-0439-2

Lee, J., Lee, H., Park, H., Cho, G., Kim, D., & Cho, J. (2021). Design optimization of a vane type pre-swirl nozzle. *Engineering Applications of Computational Fluid Mechanics*, *15*(1), 164-179. https://doi.org/10.1080/19942060.2020.1847199

Liao, G., Wang, X., & Li, J. (2014). Numerical investigation of the pre-swirl rotor–stator system of the first stage in gas turbine. *Applied Thermal Engineering*, *73*(1), 940-952. https://doi.org/10.1016/j.applthermaleng.2014.08.054

Liu, G., Gong, W., Wu, H., & Lin, A. (2021). Experimental and CFD analysis on the pressure ratio and entropy increment in a cover-plate pre-swirl system of gas turbine engine. *Engineering Applications of Computational Fluid Mechanics*, *15*(1), 476-489. https://doi.org/10.1080/19942060.2021.1884600

Luo, X., Han, G., Wu, H., Wang, L., & Xu, G. (2014). Experimental investigation of pressure loss and heat transfer in a rotor–stator cavity with two outlets. *International Journal of Heat and Mass Transfer*, *78*, 311-320. https://doi.org/10.1016/j.ijheatmasstransfer.2014.06.057

Ma, A., Wu, Q., Zhou, T., & Hu, R. (2022). Effect of inlet flow ratio on heat transfer characteristics of a novel twin-web turbine disk with receiving holes. *Case Studies in Thermal Engineering*, *34*, 101990. https://doi.org/10.1016/j.csite.2022.101990

Musthafa, M., & Ghosh, I. (2022). Spirally wound tubular heat exchanger optimisation using Genetic Algorithm. *Applied Thermal Engineering*, *215*, 118956. https://doi.org/10.1016/j.applthermaleng.2022.118956

Owen, J. M., & Pincombe, J. R. (1980). Velocity measurements inside a rotating cylindrical cavity with a radial outflow of fluid. *Journal of Fluid Mechanics*, *99*(1), 111-127. https://doi.org/10.1017/S0022112080000547

Owen, J. M., Pincombe, J. R., & Rogers, R. H. (1985). Source–sink flow inside a rotating cylindrical cavity. *Journal of Fluid Mechanics*, *155*, 233-265.

https://doi.org/10.1017/S0022112085001793

Shen, W., & Wang, S. (2022). Large eddy simulation of turbulent flow and heat transfer in a turbine disc cavity with impellers. *International Communications in Heat and Mass Transfer*, *139*, 106463. https://doi.org/10.1016/j.icheatmasstransfer.2022.106463

Sun, W. J., Wang, Y. J., Zhang, J. Z., & Gao, Q. H. (2023). Genetic optimization of longitudinal ribs on comprehensive heat transfer performance in hollow rotor within axial through flow. *International Communications in Heat and Mass Transfer*, *144*, 106782. https://doi.org/10.1016/j.icheatmasstransfer.2023.106782

Taguchi, G. (1986). *Introduction to quality engineering: designing quality into products and processes*. Asian Productivity Organization. https://doi.org/10.1002/QRE.4680040216

Tang, H., Deveney, T., Shardlow, T., & Lock, G. D. (2022). Use of Bayesian statistics to calculate transient heat fluxes on compressor disks. *Physics of Fluids*, *34*(5). https://doi.org/10.1063/5.0091371

Unnikrishnan, U., & Yang, V. (2022). A review of cooling technologies for high temperature rotating components in gas turbine. *Propulsion and Power Research*, *11*(3), 293-310. https://doi.org/10.1016/j.jppr.2022.07.001

Wilamowski, B. M., & Irwin, J. D. (Eds.). (2018). *Intelligent systems*. CRC press. https://doi.org/10.1201/9781315218427

Xia, Z. L., Wang, S. F., & Zhang, J. C. (2020). A novel design of cooling air supply system with dual row pre-swirl nozzles. *Journal of Applied Fluid Mechanics*, *13*(4), 1299-1309. https://doi.org/10.36884/jafm.13.04.30957

Xu, G., Zhuang, L., Dong, B., Liu, Q., & Wen, J. (2020). Optimization design with an advanced genetic algorithm for a compact air-air heat exchanger applied in aero engine. *International Journal of Heat and Mass Transfer*, *158*, 119952. https://doi.org/10.1016/j.ijheatmasstransfer.2020.119952

Zhang, F., Wang, X., & Li, J. (2016a). Numerical investigation on the flow and heat transfer characteristics in radial pre-swirl system with different fillet radius at the junction of inlet cavity and nozzle. *Applied Thermal Engineering*, *106*, 1165-1175. https://doi.org/10.1016/j.applthermaleng.2016.06.117

Zhang, F., Wang, X., & Li, J. (2016b). Numerical investigation of flow and heat transfer characteristics in radial pre-swirl system with different pre-swirl nozzle angles. *International Journal of Heat and*

Mass Transfer, *95*, 984-995. https://doi.org/10.1016/j.ijheatmasstransfer.2016.01.010

Zhang, G., & Ding, S. (2012). Safety analysis of flow parameters in a rotor-stator cavity. *Chinese Journal of Aeronautics*, *25*(6), 831-838.

https://doi.org/10.1016/S1000-9361(11)60452-4

Zhang, K., Wang, S., Hou, X., & Wei, G. (2020). Influence of slit type receiver holes on radial pre-swirl system. *Journal of Aerospace Power*, *35*, 983-991. (In Chinese) https://doi.org/10.13224/j.cnki.jasp.2020.05.010